1 **Drought-induced vertical displacements and water loss in the Po river basin**

2 **(Northern Italy) from GNSS measurements**

3 **F. Pintori[1], E. Serpelloni[1]**

4 [1]Istituto Nazionale di Geofisica e Vulcanologia (INGV), Bologna, 40128, Italy.

5 Corresponding author: Francesco Pintori (francesco.pintori@ingv.it)

6 **Key Points:**

7 • Vertical ground displacements are used as an independent measure of terrestrial water
8   storage variations.

9 • Interannual changes of vertical displacements are a reliable near real-time indicator of
10   drought severity.

11 • The inversion of GNSS displacements shows that about 70 billion tons of water is lost
12   during the 2021-2022 drought in the Po river basin.

13

14

15 **Abstract**

16 We study vertical ground displacement time series from GNSS stations to measure deformation
17 associated with hydrological drought in the Po river basin. Focusing on interannual trend
18 changes, rather than seasonal (annual) components, we found a clear spatially correlated
19 deformation signal that is temporally (anti)correlated with changes in the Po river level and the
20 SPEI-12 drought index, with stations moving upward during periods of river/index level
21 decrease and vice versa. In the 2021-2022 time span, which culminated in the most severe
22 drought of the last two centuries, we estimate the amount and spatial distribution of water loss in
23 the basin and its surroundings. Excluding the seasonal signals, between January 2021 and August
24 2022, the GNSS stations underwent uplift, up to 7 mm, which corresponds to ~70 Gtons of water
25 loss. Compared to GLDAS and GRACE estimates, GNSS results show a similar temporal
26 evolution of water content but a more heterogeneous distribution of values. Dense GNSS
27 networks provide an effective way to monitor multiannual trend changes in water storage even in
28 small water basins and serve as a reliable indicator of drought severity.

29 **Plain Language Summary**

30 This study looks at the way the ground moves up and down in the Po river basin, in northern
31 Italy, using Global Navigation Satellite System (GNSS) stations. We measure how much water
32 was lost during a big drought in the area, which occurred from January, 2021 to August, 2022.
33 During this time interval, the GNSS stations show that the ground mostly moved upwards, which
34 means that water was being lost. Besides the annual water storage variations, we estimate that
35 about 70 billion tons was lost during that time, in agreement with other ways of measuring
36 terrestrial water variations. This study shows that GNSS stations can be an alternative way to
37 measure how much water is being lost during drought in small areas and common vertical
38 displacement signals are a good approximation of drought indexes.

39

40

1 Introduction

Drought is one of the most complex recurring natural disasters, defined by a deficiency of precipitations that causes prolonged water scarcity. Failure to manage drought risk has the potential to have dire consequences for people, livelihoods, economy and ecosystems. During the summer of 2022, Italy faced the most severe drought in the last two centuries, where the dry conditions were related to several drivers, the most relevant being the changes in the precipitation regime, resulting in a decline of snow fraction and snowmelt, and an increasing evaporation rate (Montanari et al., 2023). The drought significantly impacted the largest Italian river, the Po, whose level has significantly decreased from the summer of 2021 to the autumn of 2022 (Fig. 1). In summer 2022 several regions declared a state of emergency, and drinking water has been rationed in hundreds of municipalities in northern Italy.
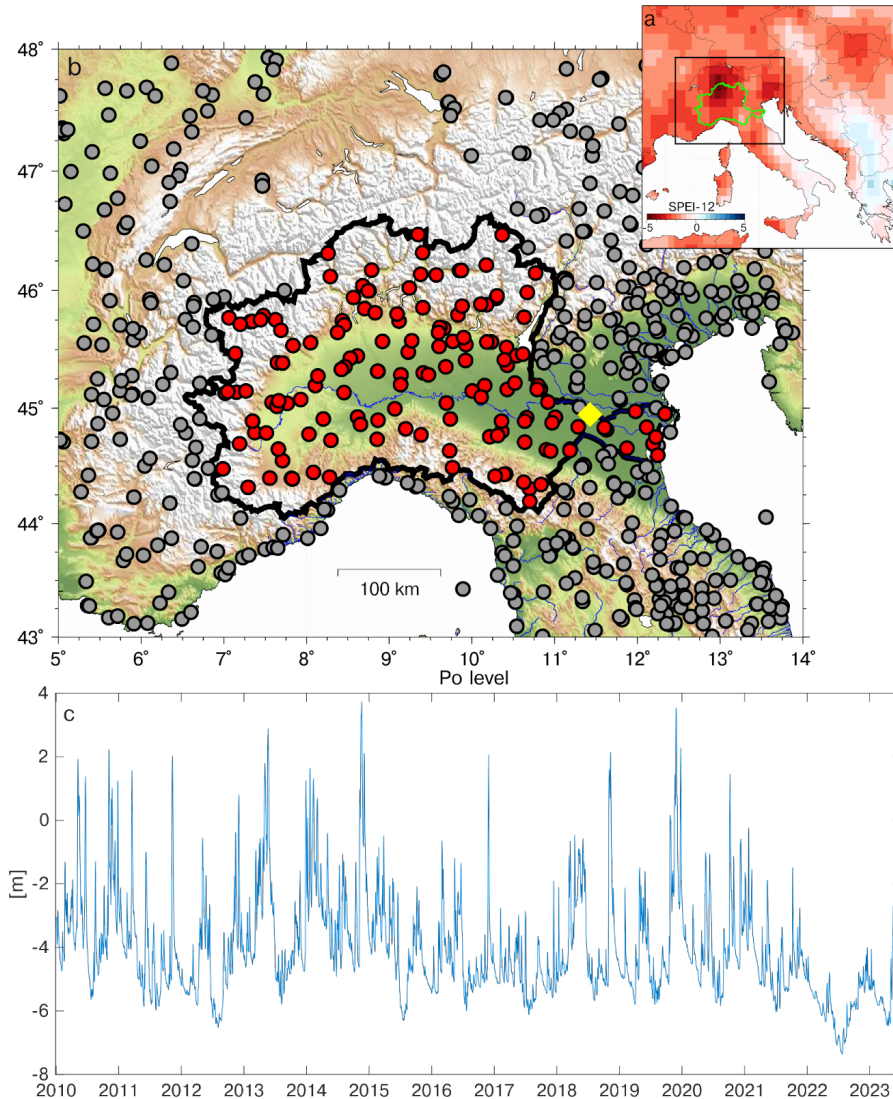
Figure 1. a) Map of the SPEI-12 values at August 2022. b) The study area: the black line represents the Po river (thick blue line) basin; the dots show the positions of the GNSS stations used in the analysis, the reds are the ones inside the basin, the gray the ones outside; the yellow diamond shows the location of the Po level measurement point. c) Po river level changes.

The effects of droughts are particularly dangerous in the Po river basin, which has an extension of ~74·10^4 km^2, for various reasons: drought threatens the crops in the Po Valley, which are around 40% of the total food produced in Italy, and impacts energy production, since a reduced river flow causes deficiencies in hydropower generation and cooling of thermal plants (Boyko et al., 2022).

Due to global warming, more frequent, longer and severe droughts are likely to occur in the future (Boyko et al., 2022). In order to evaluate the best policies to address the problems caused by water scarcity, it is crucial to measure and monitor variations in terrestrial water storage (TWS). For drought monitoring, in fact, changes or anomalies in TWS provide direct observations of total water availability, complementing model-based measures such as drought severity indices. Taking into account the anomalies of both precipitation and potential evapotranspiration, Vicente-Serrano et al. (2010) proposed the Standardised Precipitation-Evapotranspiration Index (SPEI) drought index. In particular, the SPEI-12 quantifies the drought level of the previous 12 months, considering the precipitation and potential evapotranspiration anomalies over 12 months (Fig. 1a). However, meteorological drought indices, such as the SPEI, and other drought indices, like the Standardized Precipitation Index (SPI) or the Palmer Drought Severity Index (PDSI), estimate droughts based on precipitation and temperature anomalies, so they do not allow to quantify TWS anomalies. TWS, in general, is hard to quantify because it is the sum of many components, including groundwater, surface water, vegetation and soil moisture, ice and snow. Piezometers, for example, effectively monitor groundwater level variations but not the other water storage components, and evaluating the water volume changes from them is not straightforward. On the other hand, the Global Land Data Assimilation System (GLDAS) model provides daily variations of the soil moisture and snow water equivalent, but it can not take into account the groundwater stored more than 2 m below the surface (Argus et al., 2014; Jiang et al., 2021). Geodetic techniques have a distinctive role in monitoring the hydrological cycle, as they are the sole means of directly observing TWS anomalies and they can

84   function across local to global scales. TWS anomalies can be estimated at global scale by using

85   Gravity Recovery and Climate Experiment (GRACE) measurements, which allow modeling

86   water storage changes by inverting the spatiotemporal variations of the Earth's gravity field.

87   Unlike GLDAS, GRACE accounts for all the components of TWS, but it provides a spatial

88   resolution of ~300-400 kilometers, which is insufficient for monitoring smaller watersheds (Fu et

89   al., 2015; Knappe et al., 2019), particularly in mountainous regions where TWS gradients are

90   steep, as highlighted in Argus et al. (2017). Moreover, due to the monthly nature of GRACE

91   observations they are not suitable for assessing water availability and flood risk during and

92   following brief, intense precipitation events.

93   TWS variations are indirectly detectable not only through gravity data but also by

94   measuring ground deformation through geodetic observations: an increase of the water content,

95   in the absence of poroelastic processes, causes an increasing load on the Earth surface, which

96   subsides elastically; while when the water content decreases the crust moves upward because of

97   the water content decrease. Global Navigation Satellite System (GNSS) measurements, for

98   example, provide daily measurements of ground displacements, at mm precisions, that can be

99   used to measure ground deformation associated with TWS variations. Argus et al. (2014)

100   inferred the spatial distribution of the TWS seasonal amplitude, expressed in terms of equivalent

101   water height (EWH), by inverting the seasonal vertical displacements of the ground in

102   California. Fu et al. (2015) estimated TWS variations from GNSS measurements of vertical

103   displacement in Washington and Oregon, finding that the largest seasonal variations of water

104   content were localized in the mountain areas. GNSS displacements have been inverted to

105   estimate the TWS also by Jin and Zhang (2016) in the southwestern United States, by Zhang et

106   al. (2016) over the Yunnan Province in China and by Ferreira et al. (2019) in the entire South

107   America.

108   Carlson et al. (2022) computed TWS in California using a joint inversion method

109   combining the GRACE products with the results of the inversion of GNSS data, taking

110   advantage of the dense spatial distribution of GNSS data together with GRACE's ability to

111   provide regional closure of the water budget. While most of the above mentioned studies dealt

112   with seasonal fluctuations of TWS, here we focus on multi-annual trends. We model

113   displacement time-series looking for trend changes in the vertical component, with the goal of

114   studying the non-seasonal deformation signals caused by interannual TWS variations, similarly

115   to Borsa et al. (2014), focusing in particular on the most recent and severe 2021-2022 drought.

116   In Section 2 we describe the GNSS data used and the methods applied to analyze the

117   vertical displacement time series; in Section 3 we show the relationship between geodetic and

118   hydrological observations and provide a quantitative estimation of the evolution of the TWS. In

119   Section 4 we discuss the results, in light of alternative estimates of water storage variations.

120   **2 Data and Methods**

121   We consider ~180 daily GNSS vertical ground displacement time series from January,

122   2010 to June, 2023 of continuous stations located in the Po river basin (see Fig. 1). We also

123   include in the analysis ~280 stations located within 1° of the catchment limits in order to reduce

124   inversion artifacts near the boundaries of the study region (Fu et al. 2015). This is part of a larger

125   geodetic solution encompassing the whole Euro-Mediterranean region, obtained following the

126   approach detailed in Serpelloni et al. (2022). We remove the long-term linear trend from the time

127   series using the Median Interannual Difference Adjusted for Skewness (MIDAS) estimator

128   (Blewitt et al. 2016) and filter the contribution of the non-tidal atmospheric loading (NTAL), as

129   suggested by White et al. (2022), since they can produce displacements of several millimeters at

130   daily-weekly timescales that can interfere with the hydrological signal. The NTAL-induced

131   vertical displacements are evaluated from the daily 0.5° x 0.5° gridded solution of the Earth-

132   System-Modeling Group at the German Research Center for Geosciences (Dill and Dobslaw,

133   2013) and its contribution in each site is calculated considering the nearest grid point where the

134   displacements associated with NTAL are computed. The resulting GNSS vertical displacements

135   time series are then analyzed using a trend filtering approach, which performs an extensive

136   analysis using a L1 norm regularization model to identify the seasonal components, offsets and

137   linear trend changepoints in the GNSS time series (Wu et al. 2018). The piecewise trend x is

138   estimated   by   minimizing   the   weighted   sum   objective   function:

139    $(1/2)\left\| y - x - s - w \right\|_2^2 + \lambda \left\| D^{(2)} x \right\|_1 + \rho \left\| D^{(1)} w \right\|_1$

140   where y is the original time series, w indicates the level component associated with the offsets, s

141   is the seasonal term, $\left\| . \right\|_1$ represents the L1 norm and $D^{(n)}$ are the n-th difference matrix defined

142   as in Wu et al. (2018). λ and ρ are positive parameters controlling the knots of the estimation

143   trend and the frequency of level shifts, respectively (we choose λ=2000 and ρ=80). Figure 2

144 shows an example of output of this analysis. Focusing on transients and interannual variations,

145 we only consider the extracted piecewise trends, not the seasonal terms having annual and semi-

146 annual frequencies. For some stations level changes (i.e., offsets) not associated with tectonic

147 events or equipment changes are highlighted, which mostly represent fast variations in ground

148 displacements (see Fig. 2 in 2012). For this reason, in the further steps we consider the piecewise

149 trend as the sum of the trend and level components. As it can be seen in Fig. 2, there is an

150 increase in uplift starting from 2021, which is a common feature in GNSS stations within the Po

151 river basin. Fig. 2e shows the stacking of the vertical piecewise trend time-series for all stations

152 analyzed, which is performed by averaging, for each epoch, the residuals of all the time series

153 resulting by removing the mean and linear trend terms. In order to better characterize the spatial

154 distribution of this deformation signal, we use a multivariate statistical approach, similarly to

155 what is used for tectonic deformation studies (Kositsky and Avouac, 2010; Gualandi et al. 2014).
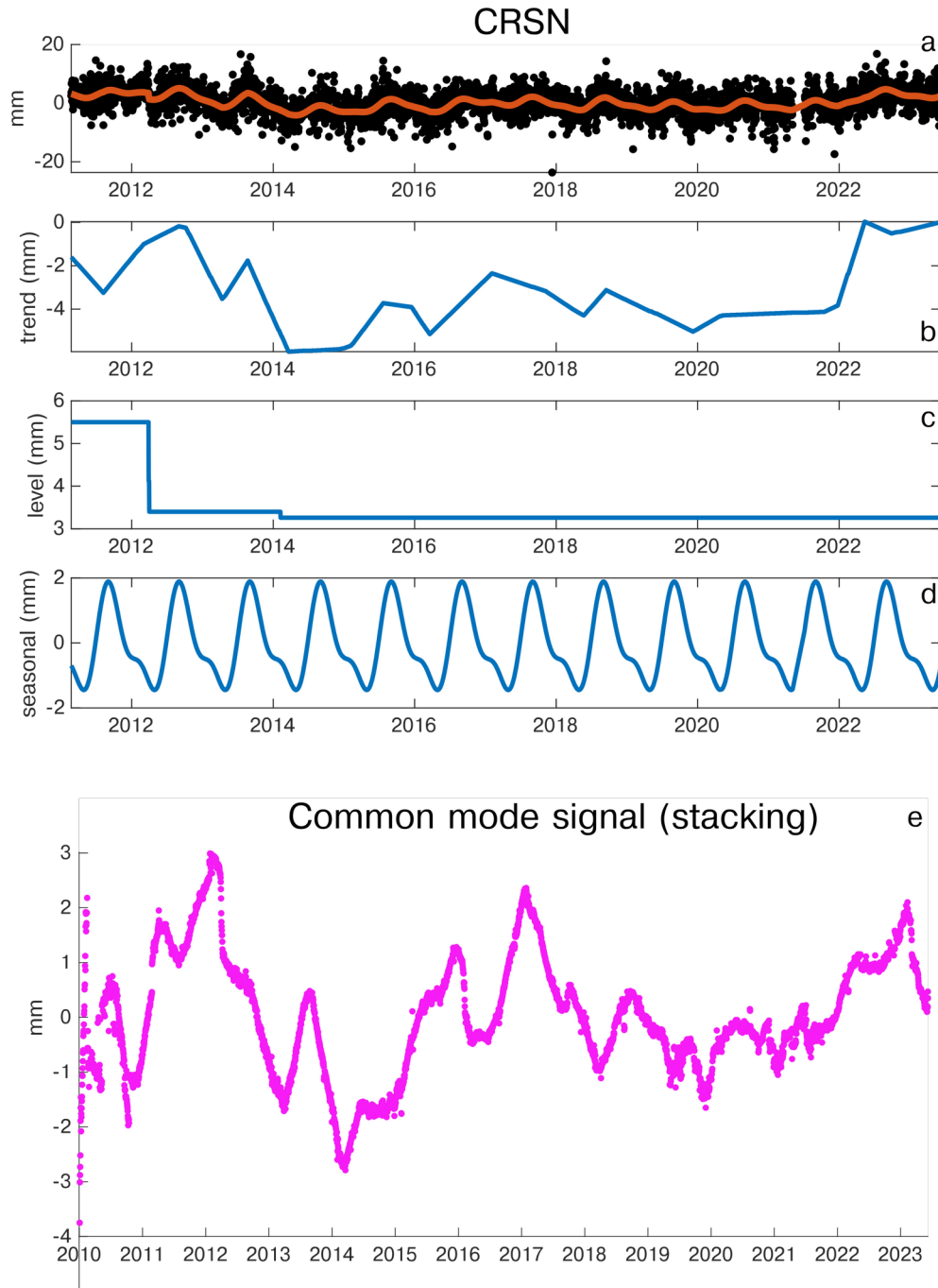
Figure 2. Example of GNSS time series decomposition performed using the L1-norm trend filtering approach. In a) the black dots represent the original time series, the red line the model obtained as the sum of the trend (b), level (c) and seasonal component (d). Panel (e) shows the result of the stacking on the piecewise vertical trends of all the stations inside the Po river basin.

162 **3 Results**

163   3.1 Comparison between geodetic and hydrological measurements

164   We adopt an approach similar to the one described in Jiang et al. (2022), using as input of

165 a principal component analysis (PCA) the piecewise vertical trends described in the previous

166 section rather than the raw time-series that also include the seasonal terms. We decompose the

167 dataset using one PC in order to identify the most important common signal of the GNSS stations

168 in the Po basin and retrieve its spatial pattern (i.e., amplitude and sign). However, the first

169 principal component (PC1) obtained performing a PCA using 2 components is almost identical to

170 the PC1 obtained performing a one-component decomposition, both in terms of temporal

171 evolution (Fig. S1) and spatial distributions (Fig. S2). The temporal evolution of PC1 (Fig. 3a)

172 well resembles the common mode signal resulting from a stacking of the vertical trend time-

173 series for all stations (Fig. 2e and Fig. S3). However, the advantage of the PCA is to provide the

174 spatial information on the displacement amplitudes (Fig. S2a). We compare the temporal

175 evolution of PC1 with the SPEI-12 index value, averaged over the Po river basin, and with the

176 Po river level measurements provided by the Regional Agency for Environmental Protection of

177 Veneto region (ARPAV; https://wwwold.arpa.veneto.it/arpavinforma/bollettini/dati-storici, Last

178 Access: 24-07-2023). The Po river level time series is filtered adopting the same approach used

179 for the GNSS time-series, retaining only the piecewise trend component (Fig. S4) and not the

180 seasonal ones. On the other hand, SPEI-12 time series does not contain annual variations, since

181 the index is computed as an anomaly over 12 months, then the time series has not been filtered.

182 Figure 3a shows that the geodetic (sign inverted), climatic and hydrological time series are

183 highly temporally correlated, so that geodetic uplift is observed coeval with the drop of the Po

184 river level and the SPEI-12 index, while the geodetic subsidence is instead observed coeval with

185 the increase of the Po river level and SPEI-12 index, respectively. Focusing on the time interval

186 covering the last drought, we observe that the three de-seasoned time series start decreasing from

187 the beginning of 2021 to mid-2022, after which they invert their sign. As a result, we set the time

188 limits of the drought as 2021.00 and 2022.58 (January 1st, 2021 - August 1st, 2022), which is

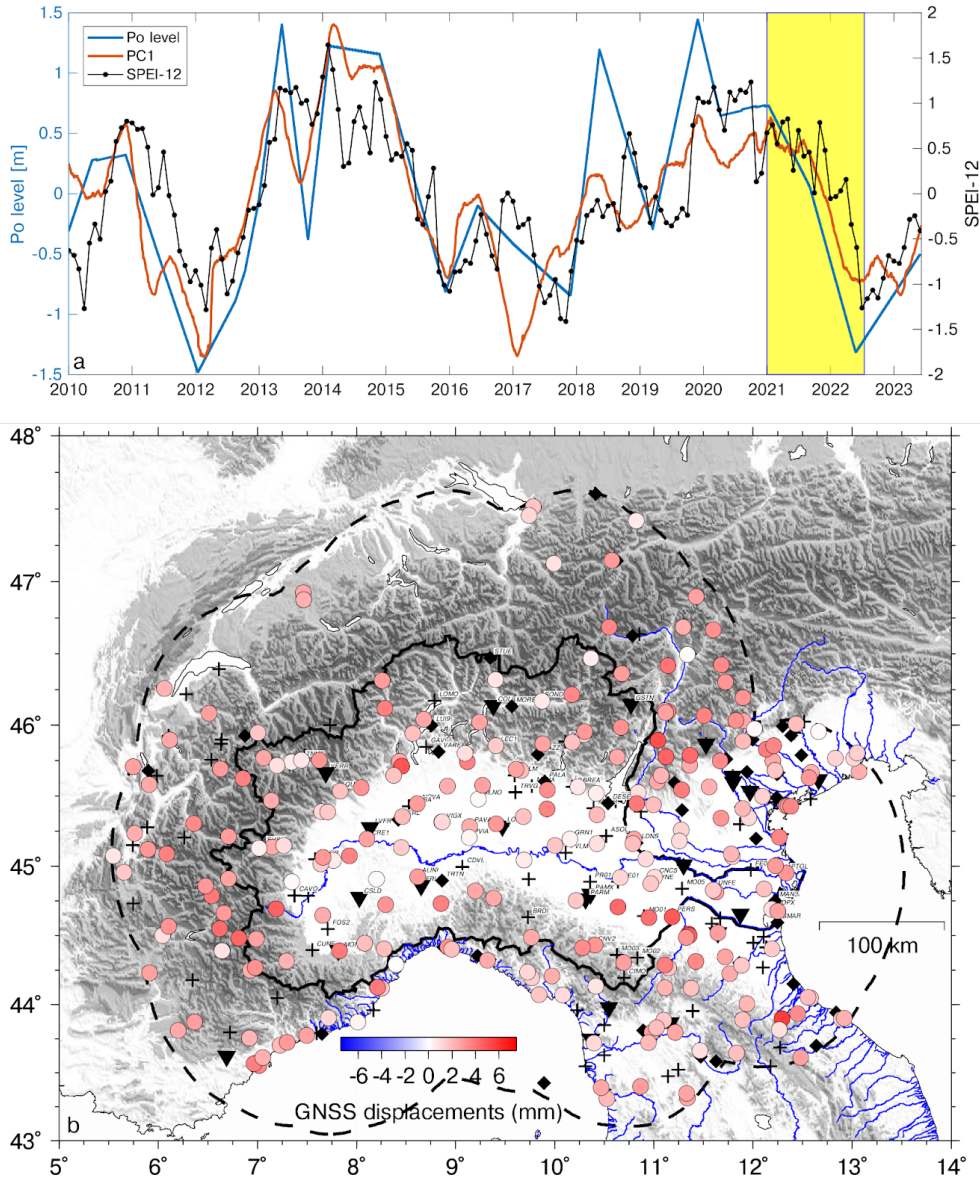189 represented as the yellow area in Fig. 3a.

Figure 3. a) Comparison between the PC1 temporal evolution, the SPEI-12 index and the Po river level. Since PC1 is obtained from detrended GNSS time series, Po river level and SPEI-12 have also been detrended for consistency. b) Vertical displacements associated with PC1 during the 2021.00 (January, 2021) - 2022.58 (August, 2022) time interval (yellow panel). The dashed line represents the boundary of the Po river basin, extended by 1°. Black triangles indicate the 22 stations excluded because they show negative displacements; black crosses represent sites with more than 75% of missing data and black diamonds the stations with no records after 2021.0.

199 The vertical displacements associated with PC1 from 2021.00 to 2022.58 are shown in Fig. 3b.
200 Most of the stations show positive values (uplift), in accordance with the hypothesis that in dry
201 periods, when the water load is reduced, the GNSS stations record uplift, while in wet periods
202 the water load increases causing a downward motion of the Earth's surface. We find that this is
203 not true for 22 sites, which show an opposite behavior (black triangles in Fig. 3b). Maximum
204 uplift, of the order of 7 mm, is observed in the south-eastern portion of the basin and in the
205 northern portion of the Po basin, which correspond to uplift rates, in the considered two years,
206 that are much faster than the long-term ones (e.g., Pintori et al., 2022).

207 3.2 Inversion of vertical ground displacements

208 The displacements associated with PC1 are inverted using the approach described in
209 Jiang et al. (2022), which estimates water storage variations assuming an elastic response of the
210 Earth to the hydrological load. In order to avoid misinterpretation of the spatial variations of the
211 water storage changes, we exclude from the inversion the 22 stations showing negative vertical
212 displacements (i.e., subsidence, Fig. S5) in the investigated time interval that, following Carlson
213 et al. (2022), are possibly affected by poroelastic processes, causing vertical displacements in the
214 opposite direction compared to the elastic ones. We also exclude from the inversion the GNSS
215 stations that have no observations recorded in the 2021.00-2022.58 time-span (i.e., do not
216 register displacements potentially associated with the last drought episode investigated in this
217 work). The total number of stations used for the inversion is then 257.

218 The relationship between the vertical displacements measured by GNSS x and the water mass
219 load u, expressed as EWH, is

220 $x = Gu$

221 where *G* is the Green's function matrix using load Love numbers of the preliminary reference
222 earth model (PREM) (Dziewonski and Anderson, 1981) as commonly used in many recent
223 works (e.g. Carlson et al. 2022, Jiang et al. 2021). The final solution for the daily estimates of
224 EWH changes u is

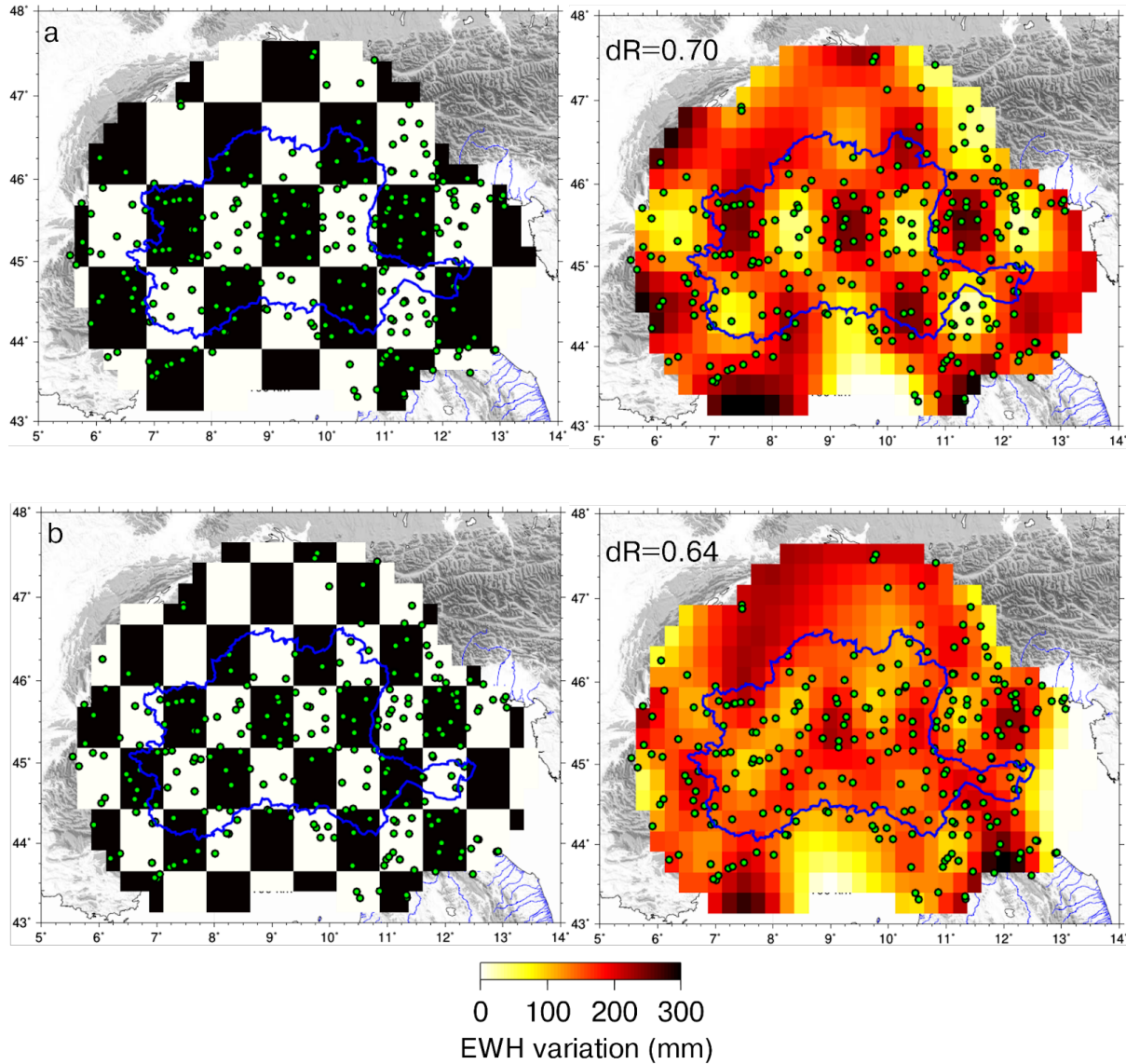225 $u = \left(G^T G + \alpha^2 L^T L\right)^{-1} G^T x$

226 where *L* is the Laplacian smoothing matrix and α is the smoothing factor controlling the relative
227 weight between model roughness and data misfit.

228 We invert the displacements associated with PC1 to estimate EWH on a 0.25°x0.25° grid. We
229 choose $\alpha = 0.0030$, which is the minimum in the line showing the relation between the sum of
230 squared residuals from cross-validation (CVSS) and the smoothing factor (Fig. S6), and use 4
231 neighbor points for calculating the Laplacian matrix during the least-squares inversion. Fig. 3a
232 shows the temporal evolution of the EWH averaged over the study area, while Fig. 3b is a map
233 of the EWH variations that occurred in the 2021.00 - 2022.58 time interval (yellow box in Fig.
234 3a).

235 A checkerboard test using synthetic inputs is performed to show the ability of the inversion
236 method and the distribution of the GNSS stations to resolve spatial features of water mass
237 variation in a checkerboard pattern, where each mass has dimensions of 1° × 1° and an EWH
238 change of 300 mm (Fig. 4a). The inversion performance is evaluated estimating the agreement
239 dR between each grid point of the checkerboard synthetic model within the Po river basin and
240 the results of the inversion (Fig. 4a) using the following equation, which estimates the percentage
241 of accuracy:

242 $dR = 1 - \dfrac{|input - output|}{max(input)}$

243   where *input* is the value of the checkerboard synthetic model, *output* the value resulting from the

244   inversion and $max(input)$ the maximum value of *input*, i.e. 300 mm.

245   The mean value of *dR* computed over all the grid points is 0.67, then we can conclude that the

246   accuracy of our inversion, at the resolution of 1° x 1°, is 67%. By using smaller patches we find

247   a rapid degradation of the spatial accuracy (Fig. 4a-b).

248

Figure 4. Checkerboard test using synthetic data. a) Comparison between the checkerboard synthetic model (left) and the results using the inversion method (right) considering a 1.00° spatial resolution. b) Same as a) but considering a 0.75° spatial resolution.

4 Discussion

253

254   We compare the EWH obtained by inverting the GNSS displacements (EWH$_{gnss}$) with
255 surface water content from GLDAS (SWC) and with Liquid Water Equivalent Thickness (LWE)
256 from GRACE. The GLDAS products provide the soil moisture content in the first 2 m of the
257 subsurface, the snow depth water equivalent, the plant canopy surface water and the root zone
258 soil moisture (Rodell et al., 2004). We consider as SWC the sum of these four components,
259 which are provided as 0.25°x0.25° gridded dataset and 3-hours temporal resolution, which are
260 transformed into daily time series by averaging the 3-hourly time series to make them consistent
261 with the daily resolution of EWH$_{gnss}$.

262   LWE is computed using the NASA Jet Propulsion Laboratory (JPL) GRACE and
263 GRACE-FO RL06 Mascon solutions (Watkins et al. 2015), but we also show the results obtained
264 using other GRACE products in the supplementary material. While the data are here analyzed in
265 a 0.25°x0.25° grid for consistency with SWC and EWH$_{gnss}$, the current resolution is 300 km. The
266 temporal resolution of LWE data is monthly and data are missing in correspondence with the gap
267 between the GRACE and GRACE-FO missions, which results in a 11 month gap, from July
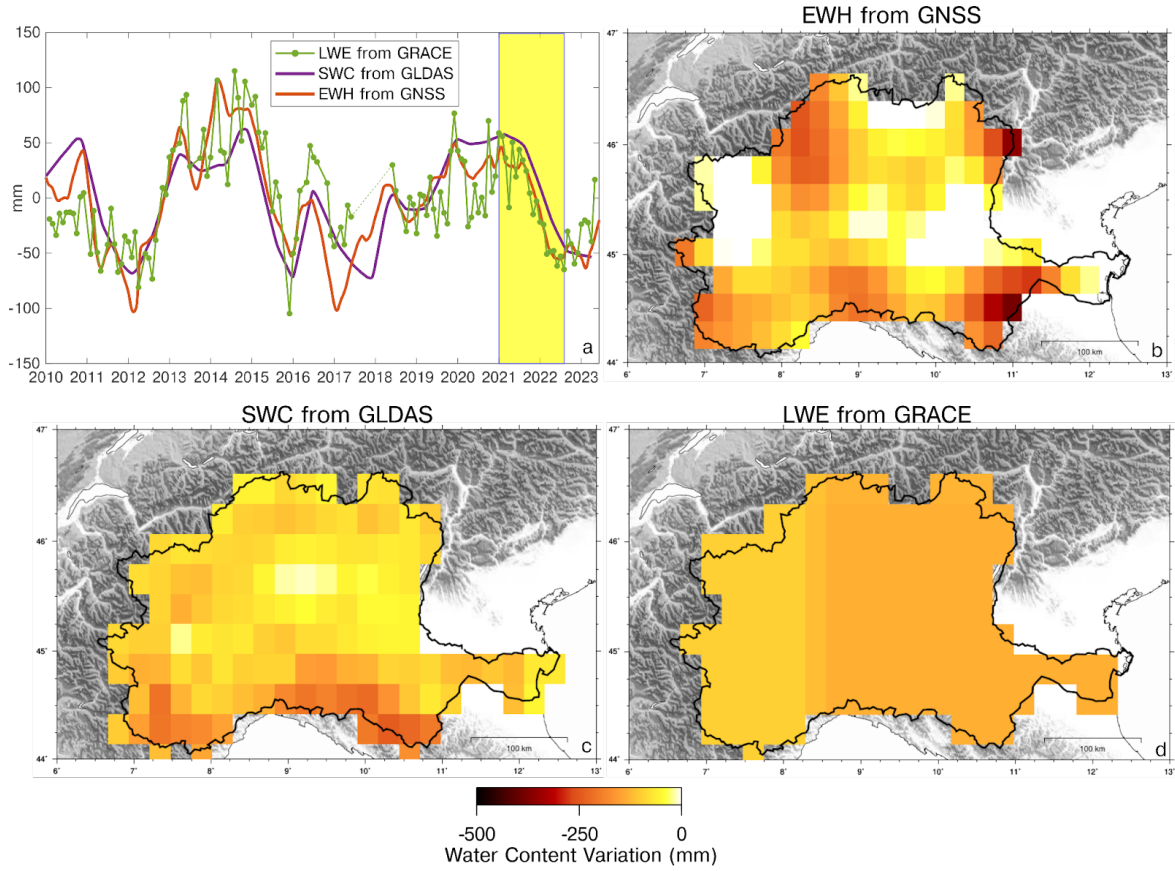268 2017 to May 2018.

269   The GLDAS products allow an estimate of the water content with a better nominal spatial
270 resolution of EWH$_{gnss}$, even though the disadvantage is that GLDAS does not take into account
271 groundwater. Importantly, while the GLDAS nominal spatial resolution is 0.25°, its effective
272 resolution may be different due to the assimilation process and the interpolation techniques used
273 to generate gridded datasets. Furthermore, the nominal spatial resolution of GLDAS may not
274 represent the true spatial variability of soil moisture in a context such as the Po river basin,
275 characterized by high topographic gradients. The correct determination of the soil types in
276 regions characterized by heterogeneous landscapes, elevation and land cover, in fact, is complex
277 and this can lead to errors in soil moisture modeling (Bi et al., 2016).
278 LWE takes into account all TWS components, but with a spatial and temporal resolution much
279 poorer than EWH$_{gnss}$. We point out that while EWH$_{gnss}$ is inverted on a 0.25°x0.25° grid, the
280 results of the checkerboard test show that the actual spatial resolution is ~1°, corresponding to
281 about 100 km (Section S1 of the Supporting Information). This is consistent with the resolution
282 achieved by Zhang et al. (2016) in the Yunnan region of China and by Fu et al. (2015) in

283   Washington and Oregon. The high spatial density of the southern California GNSS network
284   allowed Carlson et al. (2022) to reach a spatial resolution of 80 km, while when considering
285   larger study areas as in Borsa et al. (2014) and in Ferreira et al. (2019) the spatial resolution
286   decreases to 200-300 km.

287   We remove the annual and semiannual components in SWC time series using the same
288   approach used for GNSS displacement and Po river level measurements (see Fig. S7), and apply
289   a PCA using one PC on the trend components. Because of the monthly temporal resolution of the
290   GRACE products, LWE data are analyzed using a slightly different strategy: we remove the
291   annual and semiannual components from the original time series instead of estimating the trend
292   components, as done for GNSS and GLDAS time-series. As for the GLDAS and GNSS datasets,
293   the filtered time series are analyzed with a PCA with one PC. Fig. 5a shows the temporal
294   evolutions of the basin-averaged water content expressed as EWH_{gnss}, SWC from GLDAS and
295   LWE from GRACE, while Fig. 5b-d shows the spatial distributions of water loss from January,
296   2010 to August, 2022 (2021.00-2022.58, yellow box in Fig. 5a), estimated from GNSS, GLDAS
297   and GRACE, respectively. Fig. 5a shows that the drought time interval, previously defined
298   considering the SPEI-12, Po level and GNSS data, is also consistent in SWC and LWE time
299   series from GLDAS and GRACE, respectively.

300

301

Figure 5. a) Comparison among the temporal evolutions of the regional-averaged water content expressed as EWH$_{gnss}$ (red), SWC (purple) and LWE (green). Since EWH is obtained from GNSS detrended data; both GLDAS and GRACE data have also been detrended for consistency. b) Water loss occurred in the 2021.00 - 2022.58 time interval in terms of EWH from GNSS, c) SWC from GLDAS and d) LWE from GRACE.

307   The temporal evolution of the basin-averaged water content estimated by the three
308   models is very similar (Fig. 5a), suggesting that the water storage variations may be dominated
309   by its superficial content, captured by GLDAS. The spatial distribution of the water loss
310   occurring in the 2021.00 - 2022.58 time interval (Fig. 5b-d) is different depending on the
311   considered dataset; nonetheless, averaging on the Po basin surface, we obtain water loss values
312   of the order of about 69, 73 and 90 Gtons from GNSS, GLDAS and GRACE, respectively in this
313   period. Figure S8 in the supplementary material shows a comparison in terms of regional-
314   averaged water loss and spatial distribution of LWE thickness change in the 2021.00 - 2022.58
315   time interval obtained using the Gravity Information Service of the German Research Centre for
316   Geosciences (GRAVIS) and the Center for Space Research of the University of Texas (CSR)
317   GRACE products. Regional averaged water loss values according to CSR and GRAVIS products
318   are 139 and 124 Gtons, respectively. However, because of a higher temporal variability of LWE
319   values from GRACE, and in particular of CSR products, the water loss estimation may vary
320   significantly with small changes in the considered time interval.
321   The poor spatial resolution of GRACE measurements makes LWE spatial distribution
322   more uniform than the other two products and not able to detect possible concentrations of water
323   loss at the scale of the Po river basin. Both SWC and EWH_{gnss} show the largest values in the
324   southern portion of the basin, but EWH_{gnss} is large also in the north-central portion of the basin,
325   in agreement with the SPEI-12 map (Fig. 1), and very small in the eastern and western portions.
326   The reason for the observed spatial discrepancy can be a consequence of the GLDAS limitations
327   in resolving the spatial distribution of the water loss in the mountain sectors. It is also worth
328   considering that GNSS vertical displacements can contain signals that might cause an incorrect
329   estimation of the water content. In fact, the inversion is made on the displacements reconstructed
330   by the PC1. This statistical approach allows us to identify a common displacement signal that has
331   the same temporal evolution in all the GNSS stations, but different amplitudes. The amplitude
332   associated with this signal might be imprecise, especially in GNSS sites characterized by noisy
333   time-series or for stations affected by local processes.
334   Importantly, estimates of water loss values depend on the Green's function used to invert
335   the displacements data. Several authors (e.g., Argus et al., 2017; Chanard et al., 2014), point out
336   that a gravitating, spherical Earth model is preferred in this context, since non gravitating, half-
337   space models, can understate elastic vertical displacements up to a factor of 2.5. Moreover, the

338 results are not very sensitive to the Earth's structure: assuming two different models for the

339 Earth, PREM and the Gutenberg Bullen A Earth structure (Farrell, 1972), Argus et al. (2017) find

340 that the difference between the displacements caused by a 450 km × 60 km load is only 4%.

341 **5 Conclusions**

342   We analyze vertical ground displacements from GNSS stations located in the Po river

343 basin, a significant European district with industrial and agricultural settlements. We find that

344 inter-annual and multi-annual changes in vertical trends clearly respond to meteo-climatic

345 forcing and serve as a reliable, near real-time, independent approximation of drought indexes.

346 Differently from meteorological drought indicators, the measure of vertical displacements allows

347 estimating the severity of drought in terms of spatial and temporal evolution of water volume

348 loss, which is crucial for managing the problem of water scarcity. During the last dry period that

349 has affected the study region, from the beginning of 2021 to the summer of 2022, we observe a

350 regional uplift signal. This uplift reaches values of up to 7 mm and exhibits spatial variations

351 across the area. We interpret this phenomenon as a result of variable water loss and subsequent

352 reduced load, enabling us to estimate the spatial distribution of EWH. We estimate that

353 approximately 70 Gtons of water was lost in the Po river basin from 2021 to August 2022. This

354 estimate aligns with values obtained from GLDAS but is lower than the estimate derived from

355 GRACE. Additionally, while the temporal evolution of EWH estimated by GNSS, GLDAS, and

356 GRACE shows similarities, the spatial patterns differ significantly.

357   Our findings are also relevant for studying active tectonics and geodynamics. The

358 Apennines and Alps, in fact, exhibit long-term uplift signals resulting from various multiscale

359 processes (Sternai et al., 2019). Accounting for the hydrological origins of trend variations is

360 crucial to improve accuracy and prevent misinterpretation of transient signals or biases in

361 velocity estimates, especially in case of short time-series.

362   Future works will integrate GNSS with InSAR data to improve the spatial resolution of

363 EWH to a few tens of meters, as demonstrated by Ghorbani et al. (2022). This integration would

364 enhance our understanding of the phenomenon and provide more detailed information on water

365 loss and recharge dynamics.

366

372 **Open Research**

373   The EWH is estimated by inverting the GNSS data using the GNSS2TWS software

374 (https://github.com/jzshhh/gnss2tws).

375   The trend filtering on the GNSS vertical displacements time series is performed using the

376 L1tool software (https://github.com/wudingcheng/l1tool).

377   The stacking of the GNSS time series is performed using the GNSS_TS_NRS code

378 (https://github.com/CL-Xiong/GNSS-TS-NRS, He et al., 2020).

379   GLDAS   data   was   downloaded   from

380 https://disc.gsfc.nasa.gov/datasets/GLDAS_NOAH025_3H_2.1/summary?keywords=GLDAS.

381   GRACE data was downloaded from http://www2.csr.utexas.edu/grace.

382   SPEI-12   data   was   downloaded   from

383 https://spei.csic.es/map/maps.html#months=1#month=0#year=2023GNSS.

384   GNSS   time   series   data   are   available   from

385 https://doi.pangaea.de/10.1594/PANGAEA.958598.

386   The maps have been made using the GMT software (Wessel et al. 2019).

387 **References**

388 Argus, D. F., Fu, Y., & Landerer, F. W. (2014). Seasonal variation in total water storage in

389   California inferred from GPS observations of vertical land motion. Geophysical Research

390   Letters, 41(6), 1971–1980. https://doi.org/10.1002/2014GL059570

391 Argus, D. F., Landerer, F. W., Wiese, D. N., Martens, H. R., Fu, Y., Famiglietti, J. S., et al.

392   (2017). Sustained water loss in California's mountain ranges during severe drought from

393   2012 to 2015 inferred from GPS. Journal of Geophysical Research: Solid Earth, 122(12),

394   10,559-10,585. https://doi.org/10.1002/2017JB014424

395 Beaudoing, H. & Rodell, M. NASA/GSFC/HSL (2020), GLDAS Noah Land Surface Model L4

396   3 hourly 0.25 x 0.25 degree V2.1, Greenbelt, Maryland, USA, Goddard Earth Sciences Data

397   and   Information   Services   Center   (GES   DISC),   Accessed: [10/10/2022],

398   https://doi.org/10.5067/E7TYRXPJKWOQ

399 Bi, H., Ma, J., Zheng, W., & Zeng, J. (2016). Comparison of soil moisture in GLDAS model
400   simulations and in situ observations over the Tibetan Plateau. Journal of Geophysical
401   Research: Atmospheres, 121(6), 2658–2678. https://doi.org/10.1002/2015jd024131

402 Blewitt, G., Kreemer, C., Hammond, W. C., & Gazeaux, J. (2016). MIDAS robust trend
403   estimator for accurate GPS station velocities without step detection. Journal of Geophysical
404   Research. Solid Earth, 121(3), 2054–2068. https://doi.org/10.1002/2015JB012552

405 Boyko, O., Reggiani, P., & Todini, E. (2022). Post-processing climate projections of
406   precipitation for the Po river basin: will Italy's North become water-constrained? Hydrology
407   Research, 53(11), 1414–1427. https://doi.org/10.2166/nh.2022.063

408 Carlson, G., Werth, S., & Shirzaei, M. (2022). Joint inversion of GNSS and GRACE for
409   terrestrial water storage change in california. Journal of Geophysical Research. Solid Earth,
410   127(3), e2021JB023135. https://doi.org/10.1029/2021JB023135

411 Chanard, K., Avouac, J. P., Ramillien, G., & Genrich, J. (2014). Modeling deformation induced
412   by seasonal variations of continental water in the Himalaya region: Sensitivity to Earth
413   elastic structure. Journal of Geophysical Research: Solid Earth, 119(6), 5097–5113.
414   https://doi.org/10.1002/2013JB010451

415 Dill, R., & Dobslaw, H. (2013). Numerical simulations of global-scale high-resolution
416   hydrological crustal deformations. Journal of Geophysical Research: Solid Earth, 118(9),
417   5008–5017. https://doi.org/10.1002/jgrb.50353

418 Dziewonski, A. M., & Anderson, D. L. (1981). Preliminary reference Earth model. Physics of
419   the Earth and Planetary Interiors, 25(4), 297–356. https://doi.org/10.1016/0031-
420   9201(81)90046-7

421 Farrell, W. E. (1972). Deformation of the Earth by Surface Loads. REVIEWS OF
422   GEOPHYSICS AND SPACE PHYSICS, 10(3), 761–797.

423 Ferreira, V., Ndehedehe, C., Montecino, H., Yong, B., Yuan, P., Abdalla, A., & Mohammed, A.
424   (2019). Prospects for imaging terrestrial water storage in south america using daily GPS
425   observations. Remote Sensing, 11(6), 679. https://doi.org/10.3390/rs11060679

426 Fu, Y., Argus, D. F., & Landerer, F. W. (2015). GPS as an independent measurement to estimate
427   terrestrial water storage variations in Washington and Oregon. Journal of Geophysical
428   Research: Solid Earth, 120(1), 552–566. https://doi.org/10.1002/2014JB011415

429   Ghorbani, Z., Khosravi, A., Maghsoudi, Y., Mojtahedi, F. F., Javadnia, E., & Nazari, A. (2022).

430   Use of InSAR data for measuring land subsidence induced by groundwater withdrawal and

431   climate change in Ardabil Plain, Iran. Scientific Reports, 12(1), 13998.

432   https://doi.org/10.1038/s41598-022-17438-y

433   Gualandi, A., Serpelloni, E., & Belardinelli, M. E. (2014). Space-time evolution of crustal

434   deformation related to the Mw 6.3, 2009 L'Aquila earthquake (central Italy) from principal

435   component analysis inversion of GPS position time-series. Geophysical Journal

436   International, 197(1), 174–191. https://doi.org/10.1093/gji/ggt522

437   Gualandi, A., Serpelloni, E., & Belardinelli, M. E. (2016). Blind source separation problem in

438   GPS time series. Journal of Geodesy, 90(4), 323–341. https://doi.org/10.1007/s00190-015-

439   0875-4

440   He, X., Yu, K., Montillet, J.-P., Xiong, C., Lu, T., Zhou,S., Ma, X., Cui, H., & Ming, F. (2020).

441   GNSS-TS-NRS: An Open-Source MATLAB-Based GNSS Time Series Noise Reduction

442   Software, Remote Sensing (Basel), 12, 3532.

443   https://doi.org/10.3390/rs12213532

444   Jiang, Z., Hsu, Y.-J., Yuan, L., & Huang, D. (2021). Monitoring time-varying terrestrial water

445   storage changes using daily GNSS measurements in Yunnan, southwest China. Remote

446   Sensing of Environment, 254, 112249. https://doi.org/10.1016/j.rse.2020.112249

447   Jiang, Z., Hsu, Y.-J., Yuan, L., Feng, W., Yang, X., & Tang, M. (2022). GNSS2TWS: an open-

448   source MATLAB-based tool for inferring daily terrestrial water storage changes using

449   GNSS vertical data. GPS Solutions, 26(4), 114. https://doi.org/10.1007/s10291-022-01301-8

450   Jin, S., & Zhang, T. (2016). Terrestrial Water Storage Anomalies Associated with Drought in

451   Southwestern USA from GPS Observations. Surveys in Geophysics, 37(6), 1139–1156.

452   https://doi.org/10.1007/s10712-016-9385-z

453   Knappe, E., Bendick, R., Martens, H. R., Argus, D. F., & Gardner, W. P. (2019). Downscaling

454   vertical GPS observations to derive watershed-scale hydrologic loading in the northern

455   rockies. Water Resources Research, 55(1), 391–401.

456   https://doi.org/10.1029/2018WR023289

457   Kositsky, A. P., & Avouac, J. P. (2010). Inverting geodetic time series with a principal

458   component analysis-based inversion method. Journal of Geophysical Research, 115(B3).

459   https://doi.org/10.1029/2009JB006535

Montanari, A., Nguyen, H., Rubinetti, S., Ceola, S., Galelli, S., Rubino, A., & Zanchettin, D. (2023). Why the 2022 Po River drought is the worst in the past two centuries. Science Advances, 9(32), eadg8304. https://doi.org/10.1126/sciadv.adg8304

Pintori, Francesco; Serpelloni, Enrico (2023): Vertical displacement time series from GNSS stations in the Po river basin area [Dataset]. PANGAEA, https://doi.pangaea.de/10.1594/PANGAEA.958598

Pintori, F., Serpelloni, E., & Gualandi, A. (2022). Common-mode signals and vertical velocities in the greater Alpine area from GNSS data. Solid Earth, 13(10), 1541–1567. https://doi.org/10.5194/se-13-1541-2022

Rodell, M., Houser, P. R., Jambor, U., Gottschalck, J., Mitchell, K., Meng, C. J., et al. (2004). The global land data assimilation system. Bulletin of the American Meteorological Society, 85(3), 381–394. https://doi.org/10.1175/BAMS-85-3-381

Save, H., Bettadpur, S., & Tapley, B. D. (2016). High-resolution CSR GRACE RL06 mascons Version 2. Journal of Geophysical Research: Solid Earth, 121(10), 7547–7569. https://doi.org/10.1002/2016JB013007

Save, H. (2020). "CSR GRACE and GRACE-FO RL06 Mascon Solutions v02", https://doi.org/10.15781/cgq9-nh24

Serpelloni, E., Cavaliere, A., Martelli, L., Pintori, F., Anderlini, L., Borghi, A., et al. (2022). Surface Velocities and Strain-Rates in the Euro-Mediterranean Region From Massive GPS Data Processing. Frontiers in Earth Science, 10. https://doi.org/10.3389/feart.2022.907897

Sternai, P., Sue, C., Husson, L., Serpelloni, E., Becker, T. W., Willett, S. D., et al. (2019). Present-day uplift of the European Alps: Evaluating mechanisms and models of their relative contributions. Earth-Science Reviews, 190, 589–604. https://doi.org/10.1016/j.earscirev.2019.01.005

Toreti, A., Bavera, D., Avanzi, F., Cammalleri, C., De Felice, M., de Jager, A., et al. (2022). Drought in northern Italy March 2022 : GDO analytical report. Publications Office of the European Union. https://doi.org/10.2760/781876

Vicente-Serrano, S. M., Beguería, S., & López-Moreno, J. I. (2010). A Multiscalar Drought Index Sensitive to Global Warming: The Standardized Precipitation Evapotranspiration Index. Journal of Climate, 23(7), 1696–1718. https://doi.org/10.1175/2009JCLI2909.1

490   Watkins, M. M., D. N. Wiese, D.-N. Yuan, C. Boening, & F. W. Landerer (2015). Improved
491   methods for observing Earth's time variable mass distribution with GRACE using spherical
492   cap mascons, Journal of Geophysical Research, 120, https://doi:10.1002/2014JB011547

493   Wessel, P., Luis, J. F., Uieda, L., Scharoo, R., Wobbe, F., Smith, W. H. F., & Tian, D. (2019).
494   The Generic Mapping Tools version 6. Geochemistry, Geophysics, Geosystems, 20(11),
495   5556– 5564. https://doi.org/10.1029/2019GC008515

496   White, A. M., Gardner, W. P., Borsa, A. A., Argus, D. F., & Martens, H. R. (2022). A review of
497   GNSS/GPS in hydrogeodesy: hydrologic loading applications and their implications for
498   water resource research. Water Resources Research, 58(7), e2022WR032078.
499   https://doi.org/10.1029/2022WR032078

500   Wu, D., Yan, H., & Yuan, S. (2018). L1 regularization for detecting offsets and trend change
501   points in GNSS time series. GPS Solutions, 22(3), 88. https://doi.org/10.1007/s10291-018-
502   0756-4

503   Zhang, B., Yao, Y., Fok, H. S., Hu, Y., & Chen, Q. (2016). Potential Seasonal Terrestrial Water
504   Storage Monitoring from GPS Vertical Displacements: A Case Study in the Lower Three-
505   Rivers Headwater Region, China. Sensors (Basel, Switzerland), 16(9).
506   https://doi.org/10.3390/s16091526

507   Zhang, L., Yi, S., Wang, Q., Chang, L., Tang, H., & Sun, W. (2019). Evaluation of GRACE
508   mascon solutions for small spatial scales and localized mass sources. Geophysical Journal
509   International, 218(2), 1307–1321. https://doi.org/10.1093/gji/ggz198